Seepage channel development in the crown pillar: Insights from induced microseismicity

Jingren Zhou[1], Jiong Wei[2*], Tianhong Yang[3], Penghai Zhang[3], Feiyue Liu[3], Jiankang Chen [1]

([1] State Key Laboratory of Hydraulics and Mountain River Engineering, College of Water Resources and Hydropower, Sichuan University, Chengdu 610065, China

[2] Department of Engineering Mechanics and CNMM, Tsinghua University, Beijing 100084, China

[3] Center for Rock Instability and Seismicity Research, School of Resource and Civil Engineering, Northeastern University, Shenyang 110819, China)

Abstract:

The stability of crown pillar is critical during the transition from open pit to underground mining. Mining-induced fractures in the pillar form water seepage channels, which can cause potential water inrush hazards. A microseismicity-based method to establish seepage channel network and assess damage state of rock mass in the pillar is proposed. The formation processes of seepage channels and associated rock failure mechanism were analyzed. First, the spatiotemporal evolution of the microseismic (MS) events was presented, based on which the development process of the fractured zone was determined. Second, moment tensor inversion (MTI) was utilized to interpret the focal mechanism of the MS events. A 3D rose diagram was utilized to measure the fracture orientations and determine the main fracture surfaces, and a fracture network was subsequently established. Meanwhile, the distribution characteristics of the fracture radii and volumes were discussed. The results show that shear fractures were dominant in pillar and accounted for more than 90% of all MS events. The overall damage tensor of the pillar was subsequently assessed based on the MS-derived fractures, and the maximum damage direction was determined. Third, a fast chronological expansion method was proposed to iteratively build a connected network with a combination of MS event locations and the corresponding fracture orientations. The MS-derived connected network was used to estimate the distances of event-to-event seepage, from which the shortest seepage channel from each individual event to the network is

* Corresponding author, jiong.wei@foxmail.com

determined in chronological order. Seepage channels between hydraulic recharge and discharge points were inferred. These results could be helpful for better characterization of seepage channel development and the implementation of pillar reinforcement.

Key words:

Microseismic monitoring; Crown pillar; Moment tensor inversion; Fracture network; Seepage channel

1. Introduction

A crown pillar is defined as the in-situ rock or transition region between the pit bottom and an underground opening due to a transition from open pit to underground mining [1]. Such structure is used to support the overburden and provide a safe working environment for personnel and equipment. Thus, ensuring the stability of crown pillar has become one of the most challenging problems for mines during a transition from open pit to underground mining [2]. Water seepage and buried faults are two main factors that threaten the instability of crown pillar. Many cases of water inrush have been documented in mines throughout the world. To avoid potential water inrush hazards, both the long-term monitoring of the stability of crown pillar and analysis of the formation processes of seepage channels are required.

A conventional method that is often used to assess the stability of crown pillar is the calculation of the factor of safety (FoS). The FoS is defined as the ratio of a pillar's estimated strength to the pillar's stress [3, 4]. Tributary area theory [5], numerical simulation [6] and empirical method [7] have been developed to estimate the strengths of such pillars. However, some problems still exist when calculating the FoS. First, pillars are typically irregular, and the stress in a pillar is difficult to estimate. Second, the overburden is supported by an array of pillars, but the FoS is the property of an individual pillar. Third, water seepage and discontinuous structures like faults, joints and fissures are seldom considered.

Over the last decade, several attempts have been carried out to monitor the stability of pillar. Tawadrous and Katsabanis [8] investigated the stability of crown pillar based on artificial neural networks, within which input parameters are required for training and then to predict the crown pillar behavior. In their study, the proper choice of parameters is significant and it may make substantial differences in the results. Moreover, some factors, such as the water seepage path and the distribution pattern of stopes, are difficult to describe using input parameters. Zaidel et al. [9] applied the finite difference software MODFLOW to simulate the water seepage path throughout the workings of a mine and discussed the numerical errors induced by finite-difference grids. The determination of the mechanical parameters in a numerical model is difficult but vital [10], and a large number of in-situ rock mass tests and laboratory tests are required [11]. Due to the computational limits, the numerical model must be simplified, and many factors regarding the complexity of the rock mass are consequently ignored. Meanwhile, the simulation results also highly depend on the chosen constitutive model. Although numerical methods have proven effective, differences still exist in the results. Therefore, numerical simulations should be combined with field monitoring data to reveal the actual state of rock mass.

MS monitoring is a burgeoning non-destructive field monitoring technology that has been widely used in many rock engineerings, such as tunnelling [12-14], slope control [15-18], oil and gas exploitation [19-21], underground nuclear waste repository [22, 23] and mining [24-26]. MS monitoring systems are capable of constantly detecting elastic waves in a rock mass and providing feedback on the properties of the sources of failure, including the hypocenter location and source parameters [27, 28]. Thus, it is an efficient tool for detecting buried fault dislocations and seepage channel formations, which is resulted from mining activities and occurs in deeply buried rock masses [29, 30]. Seepage paths and hydraulic sources are both important in understanding the mechanism of water inrush incidents. The conventional methods to analyze seepage channels are physical similitude modeling [31], numerical simulation and groundwater boreholes [32]. Zhao et al. [25] proposed a method to inverse the seepage channels using intersections of MS-derived fractures. This method assumes that the rock mass is strictly impermeable and water is forced to flow between fractures via their intersection points. It may underestimate the number of seepage channels for the ignorance of water seepage in rock mass. And if a fracture intersects with several fractures, there will be ill-conditioned seepage channels on fracture surfaces. Moreover, this method does not consider the chronological effect of the MS data which will significantly affect the inversion result of seepage channels.

The aim of this study is to propose a method for analyzing the development processes of seepage channels in crown pillar using MS technology. Based on the method, the spatiotemporal evolution of the MS events with moment magnitude information was presented. Then, the failure types of the MS events were discerned via MTI. The fracture orientations were measured using the proposed 3D rose diagrams. After that, the main fracture surfaces were derived. The distribution characteristics of the source radii and failure volumes were discussed. Finally, the connectivity among the MS sources was analyzed based on a proposed connected network. The formation processes of the seepage channels, seepage paths, discharge areas and hydraulic recharge sources were determined.

2. Theory of moment tensor inversion

The MS source can be mathematically represented by a moment tensor (MT), which can be calculated by the MTI method. As presented in Fig. 1, the components of the MT denote different moments at the source. A seismic source induced by rock fracturing can be expressed as a linear combination of the moments. To satisfy the moment equilibrium, MTs are usually symmetric, i.e., $M_{ij} = M_{ji}$. MTs can be used to determine the failure types of rock fractures [33] and help understand rock failure mechanism [34].

[Fig. 1 goes here]

An MT can be expressed as $\boldsymbol{GM} = \boldsymbol{u}$ [35], where $\boldsymbol{u}$ is a vector representing the far-field displacement, $\boldsymbol{M}$ is the moment tensor, and $\boldsymbol{G}$ is the Green's function. Therefore, this equation can be expanded as follows:

$$\begin{pmatrix} G_{1,1}^{1} & G_{2,2}^{1} & G_{3,3}^{1} & G_{2,3}^{1}+G_{3,2}^{1} & G_{1,3}^{1}+G_{3,1}^{1} & G_{1,2}^{1}+G_{2,1}^{1} \\ G_{1,1}^{2} & G_{2,2}^{2} & G_{3,3}^{2} & G_{2,3}^{2}+G_{3,2}^{2} & G_{1,3}^{2}+G_{3,1}^{2} & G_{1,2}^{2}+G_{2,1}^{2} \\ \vdots & \vdots & \vdots & \vdots & \vdots & \vdots \\ G_{1,1}^{N} & G_{2,2}^{N} & G_{3,3}^{N} & G_{2,3}^{N}+G_{3,2}^{N} & G_{1,3}^{N}+G_{3,1}^{N} & G_{1,2}^{N}+G_{2,1}^{N} \end{pmatrix} \begin{pmatrix} M_{11} \\ M_{22} \\ M_{33} \\ M_{23} \\ M_{13} \\ M_{12} \end{pmatrix} = \begin{pmatrix} u_1 \\ u_2 \\ \vdots \\ u_N \end{pmatrix} \tag{1}$$

where $G_{k,m}^{N}$ is the displacement along the *m* direction recorded by the *N*th sensor, and *k* is the direction of a unit-force source. Thus, ***M*** can be computed when more than six sensors are triggered.

For single-component sensors, the value of ***u*** in Eq. (1) is difficult to obtain. Thus, a relative MTI method was proposed based on experimental tests [36]. When only considering the far-field term of the *P*-phase, ***u*** can be rewritten as follows:

$$u_i = \frac{r_i r_p r_q}{4\pi v_{\mathrm{p}}^3 \rho R} M_{pq}, i, p, q = 1,2,3 \tag{2}$$

where u_i is the *P*-phase first motion with respect to the *i*th-axis, $\boldsymbol{r} = (r_1, r_2, r_3)$ represents the direction vector from the source to the sensors, *R* is the hypocentral distance and ρ is the rock density.

The sensors used at the Shirengou iron mine are recyclable and are emplaced on the surfaces of hole bottoms without concrete. Therefore, the effects of both reflection and attenuation must be considered. The motion u_0 induced by a unit-source force *f*(*t*) can be determined by the following:

$$u_0 = \frac{C_s' R_e(\boldsymbol{t},\boldsymbol{r}) \mathrm{e}^{-\alpha R}}{R} f(t) = \frac{C_s' R_e(\boldsymbol{t},\boldsymbol{r})}{R} \mathrm{e}^{-\frac{\pi f}{v_{\mathrm{p}} Q} R} f(t) \tag{3}$$

where C_s' is the sensor sensitivity, $R_c(t, r)$ is the reflection coefficient, ***t*** is the direction normal to the sensor, α is the attenuation coefficient, *Q* is the *P*-phase quality factor, and *f* is the corner frequency. The values of C_s' for each sensor are determined via calibration. Then, Eq. (1) can be rewritten as follows:

$$\begin{pmatrix} c^1 r_1^1 r_1^1 & c^1 r_2^1 r_2^1 & c^1 r_3^1 r_3^1 & c^1 2 r_2^1 r_3^1 & c^1 2 r_1^1 r_3^1 & c^1 2 r_1^1 r_2^1 \\ c^2 r_1^2 r_1^2 & c^2 r_2^2 r_2^2 & c^2 r_3^2 r_3^2 & c^2 2 r_2^2 r_3^2 & c^2 2 r_1^2 r_3^2 & c^2 2 r_1^2 r_2^2 \\ \vdots & \vdots & \vdots & \vdots & \vdots & \vdots \\ c^N r_1^N r_1^N & c^N r_2^N r_2^N & c^N r_3^N r_3^N & c^N 2 r_2^N r_3^N & c^N 2 r_1^N r_3^N & c^N 2 r_1^N r_2^N \end{pmatrix} \begin{pmatrix} M_{11} \\ M_{22} \\ M_{33} \\ M_{23} \\ M_{13} \\ M_{12} \end{pmatrix} = \begin{pmatrix} u_1 \\ u_2 \\ \vdots \\ u_N \end{pmatrix} \tag{4}$$

where $c^i = \frac{C_s'^i R_e^i(\boldsymbol{t}^i,\boldsymbol{r}^i)}{R^i} \mathrm{e}^{-\frac{\pi f_c^i}{v_{\mathrm{p}} Q} R^i}, i = 1, \ldots, N.$

The full moment tensor ***M*** of an event then can be obtained by Eq. (4). Considering the eigenvalues m_1, m_2, m_3 and orthonormal eigenvectors $\boldsymbol{e}_i = (e_{ix}, e_{iy}, e_{iz})^{\mathrm{T}}$ of the moment tensor, ***M*** can be rewritten as

$$\boldsymbol{M} = [\boldsymbol{e}_1, \boldsymbol{e}_2, \boldsymbol{e}_3]\boldsymbol{m}[\boldsymbol{e}_1, \boldsymbol{e}_2, \boldsymbol{e}_3]^{\mathrm{T}} \tag{5}$$

where $\boldsymbol{m} = \begin{bmatrix} m_1 & 0 & 0 \\ 0 & m_2 & 0 \\ 0 & 0 & m_3 \end{bmatrix}$ is the diagonalized moment tensor. Following Knopoff and Randall [37] and Fitch et al. [38], a moment tensor $\boldsymbol{m}$ can be decomposed into a double-couple (DC) components, an isotropic (ISO) components and a compensated linear vector dipole (CLVD) component:

$$\boldsymbol{m} = \boldsymbol{m}^{\mathrm{ISO}} + \boldsymbol{m}^{\mathrm{DC}} + \boldsymbol{m}^{\mathrm{CLVD}} \tag{6}$$

where $\boldsymbol{m}^{\mathrm{ISO}}$ represents a volume change in the source, and $\boldsymbol{m}^{\mathrm{DC}}$ represents double-couple shear dislocation. The complete decomposition of $\boldsymbol{m}$ is as follows:

$$\boldsymbol{m} = \frac{tr(\boldsymbol{m})}{3}\begin{bmatrix} 1 & 0 & 0 \\ 0 & 1 & 0 \\ 0 & 0 & 1 \end{bmatrix} + m_3^*(1-2\epsilon)\begin{bmatrix} 0 & 0 & 0 \\ 0 & -1 & 0 \\ 0 & 0 & 1 \end{bmatrix} + m_3^*\epsilon\begin{bmatrix} -1 & 0 & 0 \\ 0 & -1 & 0 \\ 0 & 0 & 2 \end{bmatrix} \tag{7}$$

where $tr(\boldsymbol{m}) = m_1 + m_2 + m_3$ is the trace of the moment tensor, $m_i^* = m_i - \frac{1}{3}tr(\boldsymbol{m})$ is the purely deviatoric eigenvalues of the moment tensor. Assume $|m_3^*| \geq |m_2^*| \geq |m_1^*|$, $\epsilon = -m_1^*/m_3^*$ is the ratio of the minimum eigenvalue to the maximum eigenvalue. For the deviatoric condition $\sum m_i^* = 0$, we can get $0.5 \geq \epsilon \geq 0$. Since ϵ changes from 0 to 0.5, the seismic source changes from pure DC to pure CLVD.

The ratio of the pure shear component K indicates the contribution of the maximum shear moment [36]. The ratio can be expressed as follows:

$$\begin{cases} K = k_2/\sum k_{\mathrm{i}} \\ k_1 = tr(\boldsymbol{m})/3 \\ k_2 = m_3^*(1-2\epsilon) \\ k_3 = m_3^*\epsilon \end{cases} \tag{8}$$

where k_{i} is the coefficient of each components on the right side of Eq. (7).

A fracture is classified as a shear fracture when $K > 60\%$. In contrast, fractures are classified as mixed-mode and tensile fractures when $60\% \geq K \geq 40\%$ and $K < 40\%$, respectively. Moreover, the fracture orientation $\boldsymbol{n}$ and the slip direction $\boldsymbol{l}$ can be determined by the following:

$$\begin{cases} \boldsymbol{l} = \sqrt{\frac{m_3-m_2}{m_3-m_1}}\boldsymbol{e}_3 + \sqrt{\frac{m_2-m_1}{m_3-m_1}}\boldsymbol{e}_1 \\ \boldsymbol{n} = \sqrt{\frac{m_3-m_2}{m_3-m_1}}\boldsymbol{e}_3 - \sqrt{\frac{m_2-m_1}{m_3-m_1}}\boldsymbol{e}_1 \end{cases} \tag{9}$$

where e_1 and e_3 are the corresponding eigenvectors of the moment tensor. It should be noted that $\boldsymbol{n}$ and $\boldsymbol{l}$ are changeable. An ambiguity is presented because it is hard to distinguish the real fracture direction from the slip direction.

Fig. 2 shows the focal mechanism for three types of MS sources, where the red, blue and green colors represent tension, shear and mixed-mode failure types, respectively. In the following sections, these failure types are represented by simplified beach ball diagrams in the right panel of the figure. The seismic sources can be ideally simplified as two plates. Rock fractures are caused by dislocations along the two plates, and the failure types can be differentiated via the relations among the two direction vectors ***n*** and ***l***. In the case of a tensile fracture, ***n*** and ***l*** are nearly parallel. A tensile fracture and its orientation can be seen in the tensile bench ball diagram. For a shear fracture, ***n*** is nearly perpendicular to ***l***. For ***n*** and ***l*** are changeable, there are two possible fracture planes and slip directions in a focal mechanism solution, as shown in the shear beach ball diagram. Either of them could represent the real fracture if a geological survey is not conducted for verification. Accordingly, the mixed-mode fracture type is a combination of pure tension and shear, and two possible fractures are shown in the mixed-mode beach ball.

[Fig. 2 goes here]

Ohtsu [36] suggested that the fracture volume ΔV could be obtained through the MT:

$$\Delta V = M_{kk}/[(3\lambda+2\mu)l_k n_k] \tag{10}$$

where M_{kk} is the trace of the MT, λ and μ are Lame constants, and l_k and n_k are the components of ***n*** and ***l***, respectively. The source radius r_s can be determined by the following [39]:

$$r_s = \frac{K_c v_s}{2\pi f_c} \tag{11}$$

where K_c is a constant 2.34 for the Brune model, v_s is the shear-wave velocity, and f_c is the dominant frequency of the seismic wave. For seismic sources that are assumed to be product of differential movement along plates, the thickness D of a fracture can be calculated as follows:

$$D = \frac{\Delta V}{\pi r_s^2} \tag{12}$$

3. Engineering situation and MS system

3.1 Engineering situation

The Shirengou iron mine is located approximately 90 km away from the city of Tangshan, China. It is one of the largest iron mines in China with a length of nearly 2800 m from north to south and a width of 230 m from east to west. Since 2004, the mining area has transitioned from open pit to underground mining. The yellow surface in Fig. 3 represents the open pit, the blue and brown blocks below the surface denote stopes, and the cyan, green, blue and red tunnels represent 0 m, -60 m, -120 m and -180 m drifts, respectively. The stability of the crown pillar has attracted much attention.

A typical location in the mine (shown in Fig. 4) was chosen as the study area for five important reasons. First, the slopes on either side are relatively steeper than in other places. Second, a backfill plant, which is critical for stope backfill, is constructed on the eastern slope, and the main backfill pipe is fixed on the slope surface. Third, after rain events, water gathers in the pit bottom and then seeps downward into the underground openings. The water depth in the open pit bottom is about 3 m and 16 m in the dry season and rainy season, respectively. Fourth, the crown pillar in this area is the thinnest throughout the mine. Fifth, several unrecognized and illegal mined-out areas are distributed in the study area. These reasons make the stability in the study area significantly challenging.

[Fig. 3 goes here]

[Fig. 4 goes here]

3.2 MS system profile

An MS monitoring system was established in 2006. Thirty-one sensors are installed along the strike of the mine. In this study, eleven single-component sensors and one three-component sensor contained in the study area was used to monitor microseismicity in the crown pillar (shown in Fig. 5). Three illegal goafs that have been detected (brown block) and six stopes (blue blocks) are located within the 0 m and -60 m drifts. A potential buried fault (purple surface) is highlighted. The study area was fully covered by the sensor array to ensure that the recorded signals have good quality.

[Fig. 5 goes here]

4. Data analysis and discussions

4.1 Reliability analysis

After denoising, the autoregressive Akaike information criterion (AR-AIC) method [40] or the short-term average to long-term average ratio (*STA*/*LTA*) method [41] can be applied to determine the phase arrival time. Then, MS sources can be further located via the Geiger method [42]. The location error (l_{err}) can be calculated by:

$$l_{err} = v_p t_{err} = v_p||t_0 - t_i + R_i/v_p||_2 \tag{13}$$

where t_0 is the origin time, t_i represents the *P*-wave arrival time recorded by the *i*th sensor, R_i is the distance between the MS source and the *i*th sensor, v_p is the *P*-wave velocity, and t_{err} is the time error.

We adopted MS data that occurred from October 28, 2009 to March 21, 2010. Generally, the events can be classified into five different types: blasting vibrations, mechanical vibrations (MVs), MS events, background noise (BN), and impulse voltage (IV). The MS events were manually picked based on the waveform database [43]. Thus, the reliability of those results was confirmed. The distribution of the location errors is shown in Fig. 6. From the front view, the errors in the area among the stopes varied from 5 m to 22 m. Meanwhile, the errors in the east and west were relatively high. From the side view, the errors along the buried fault and above stopes No.1 and No.2 ranged from 5 m to 15 m, which are relatively low. These higher location errors are primarily attributable to the locations of events outside of the sensor array that had less sensor coverage.

[Fig. 6 goes here]

4.2 Spatiotemporal evolution of MS events

The development process of the MS events can be divided into five stages, as shown in Fig. 7. Each row shows the distribution of cumulative events among different stages. MS events are colored and scaled according to the moment magnitude. The orange lines indicate the boundary of the event cluster. At the first stage, the events induced by mining activities occurred within two main regions. The eastern region was located in the hanging wall of the buried fault, and the western part was situated above the roof of stope No.2. The moment magnitudes in this stage were low and varied from -0.7 to -0.175. At the second stage, the two regions expanded along the buried fault. Additionally, the events started to cluster around the crown pillar (i.e., the region between the 0 m drift and the pit bottom). This region, which is located immediately under the water pool in Fig. 2, was affected by water seepage and pressure from the slope. At the third stage, the upper region developed downward, and the first two regions extended towards each other. Eight events with low moment magnitudes of -0.7 ~ -0.3 occurred above the southern sidewall of goaf No.4. This indicates that a weak hydraulic linkage formed between the goaf and the fault. At the fourth stage, the central and upper regions continued to expand, after which they became connected. The moment magnitudes in the center of this region were smaller (-0.7 ~ -0.2) while those along the edge of the region were larger, especially in the upper and lower parts (-0.7 ~ 0.1). The events were mainly clustered within the foot wall of the fault and near the east sidewall and roof of stope No.2. Six events with a low moment magnitude of -0.5 occurred near the north sidewall of goaf No.3. At the final stage, the central event region developed upward towards goaf No.3 and formed a hydraulic linkage. MS activities were very high both in the crown pillar and near the junction between the fault and the 0 m drift. Events with relatively low moment magnitudes of 0.05 ~ 0.4 were clustered throughout the lower part of the buried fault and in the roof of the -60 m drift. Twelve events with moment magnitudes of -0.6 ~ 0.17 occurred in the western portion of goaf No.3. Several smaller events with moment magnitudes of -0.7 ~ -0.6 occurred above stope No.1. The white arrows in Fig. 7 illustrate the seepage paths in the study area. Water originating from both goaf No.3 and the surface seeped downward via the buried fault and concentrated in an area located 30 m above stope No.2. Most of the water then percolated downward through the roof into stope No.2. A part of the water seeped into the -60 m drift, while the remaining quantity of water infiltrated into stope No.1.

[Fig. 7 goes here]

4.3 MT inversion analysis

MT analysis is an effective way to reveal the failure mechanism of inner rock mass. The MTs were calculated using Eqs. (1) ~ (7). The results are presented in Fig. 8. Red, blue and green beach balls represent tension, shear and mixed-mode failures, respectively. In particular, tension fractures were rare during stages III and IV. Failures are primarily compression-induced shear fractures [44, 45]. Tension fractures are mainly resulted by the subsequent propagation of fractures and the concentration of tensile stress along the roofs of openings.

During the first stage, shear fractures started to develop within the central part, especially in the foot wall. This indicates the presence of a slight dislocation in this area. Tension fractures and mixed-mode fractures occurred along the east sidewall of stope No.2, and an isolated tensile fracture was found within the crown pillar.

During stage II, coincident with the mining activities, shear fractures were observed above stope No.1 and along the east sidewall of stope No.2, which is coincident with the mining activities. Near the surface, the rock masses were subjected to waterlogging and the weights of the slopes, Thus, shear failures together with mixed-mode failures appeared. Shear and tensile fractures alternately occurred near the east sidewall of stope No.2.

During stage III, additional shear failures occurred in the crown pillar. Water seeped downward through these failures and entered the buried fault. Water intruded into the primary discontinuity, thereby inducing a decrease of its shear strength. In addition, combined with the effects of blasting disturbances, shear failure continued to occur constantly. Nascent shear fractures clustered along the roof and floor of the northern part of the 0 m drift.

During stage IV, the shear zones near the northern bottom part of goaf No.3 markedly expanded. Goaf No.3, which was 17 m wide and 93 m long with a capacity of more than 32000 m^3, was perennially flooded. Based on the distribution pattern of the shear fractures, water in the goaf seeped into the 0 m level drift from the northern corner and simultaneously infiltrated into the fault from the west side, thereby forming a secondary recharge source in the study area. Shear fractures clustered around the junction between the crown pillar and the fault. Meanwhile, the hydraulic conductivity and recharge rate increased rapidly during this period.

During stage V, shear fractures occurred within the roof of the eastern part of the -60 m level drift. The shear zone extended slightly downward. New shear failures appeared more frequently in the hanging wall than in the foot wall. Moreover, the shear dislocations became more densely spaced with greater intensities in the crown pillar.

[Fig. 8 goes here]

5. MS-derived fracture network analysis

An MT can indicate the presence of a fracture at a given location, which is illustrated in Fig. 2. For a non-tensile source (i.e., a shear or mixed-mode source), two nodal planes with normal $\boldsymbol{n}$ and $\boldsymbol{l}$ can be obtained. However, only one of them is the real fracture plane. To invert fracture normals, we must have a method that is capable of correctly distinguishing the fracture planes from the auxiliary planes. The most effective way to distinguish the fracture planes from the auxiliary planes is by geological survey. However, this method is difficult because MS fractures are incredibly small in scale and are buried within inner rock masses. Zhao et al. [25] proposed a strategy to distinguish the real fracture by comparing the traction related to stress field on two possible fracture surfaces. In the case the stress field is unspecified, stress tensor can be inverted by the focal mechanisms following the method presented by Vavryčuk [46]. In order to recover the shape ratio of the principal stresses, the trace of the stress tensor is usually assumed to be zero, i.e., $\sigma_1 + \sigma_2 + \sigma_3 = 0$, which means the ISO component $\boldsymbol{m}^{\mathrm{ISO}}$ in Eq. (6) of the moment tensor should be zero [47]. Zero ISO component indicates a pure double couple MS source. This assumption has some limitations when dealing with MS events in mines because tensile component of MS events in mines is usually larger than the natural earthquake and cannot be ignored. Thus, we proposed a straightforward method to estimate the fracture normals of events.

5.1 Implementation of a 3D rose diagram

A 3D rose diagram was developed to analyze the main orientations of the fractures. The principle used to construct a 3D rose diagram is presented in Fig. 9. The first step is to make a base sphere and divide it into small facets. These facets can take many forms, such as longitude-and-latitude grids, quadrilaterals and hexagons. For a longitude-and-latitude grid, the facet sizes will decrease closer to the poles, which may make the results appear unrealistic. Quadrilateral shapes are feasible, but they are not sufficiently uniform. Meanwhile, hexagons can form a honeycomb-like structure, which is more natural and homogeneous. The base sphere can be divided into facets with different sizes (i.e., high, normal or low resolutions) according to the requirements or the amount of vectors to be counted. The vector v_i from the sphere center to the facet center can then be calculated. Given a vector v_c, the absolute value of the minimum included angle between v_c and v_i can be determined. Then, the corresponding facet is extruded by one unit. To make the results appear conspicuous, facets are colored according to their extruded lengths.

[Fig. 9 goes here]

5.2 Inversion of fracture network

The fractures were assumed to originate from the differential dislocation of two plates (shown in Fig. 2). As discussed before, only one vector can be counted for a tensile fracture, while two vectors (i.e., two nodal planes) can be observed for a shear fracture or a mixed-mode fracture. For shear and mixed-mode fractures, it is hard to distinguish the real fracture planes ***n*** from "fake" planes ***l***. Therefore, we regard both the two vectors as the normals of fractures at first and count all fracture normals in the 3D rose diagram. The extrusion length would be the longest in the direction that has the largest amount of normal vectors. The directions with long extrusion lengths are marked as the normals of potential fracture surfaces. If more than one potential fracture surfaces are found, geological structures should be considered to determine which is the most reasonable main fracture surface.

Fig. 10 shows the 3D rose diagram of the normal vectors of fractures from 290 MS events Fractures in the hanging wall (south of the fault) and in the foot wall (north of the fault) were counted separately. The number of vectors in each direction varied from 0 to 30. Thus, the 3D rose diagrams in this case were always centrosymmetric. Two and three principal directions were observed for the hanging wall and foot wall, respectively. These results could essentially represent the buried fault.

[Fig. 10 goes here]

Based on the 3D rose diagrams, the main fracture surfaces perpendicular to the main directions were obtained, the results of which were presented in Fig. 11. For clarity, the rose diagrams and the fault were separated, and the fracture surfaces were shown using colored annuluses. The fault was subdivided into two branches, i.e., F_1 and F_2. The fracture orientations were in an NEU (north, east and up) coordinate system, and they were presented at the bottom of the figure. The table in the bottom right showed the included angles between the potential main fractures and the corresponding fault branches. In the hanging wall, the blue and golden fractures exhibited included angles of 32.7° and 26.5° with F_1, respectively. Meanwhile, in the foot wall, the green, blue and golden fractures had included angles of 60.5°, 16.6° and 34.6° with F_2, respectively. These events were induced by the activation of the faults F1 and F2 under disturbances from dynamic loadings. We assumed the mechanism for the fault dislocation and the derived MS events was similar based on the classic MTI theory [48]. The one with the smallest angle with the buried fault was chosen as the main fracture surface. Then, for each shear and mixed-mode fracture, the plane with a smaller angle with the main fracture surface was the reasonable real fracture. Thus, the two golden fractures that more effectively matched with the buried fault were assumed to be the principal fractures.

[Fig. 11 goes here]

Aki and Richards [35] suggested that the normal vector $\boldsymbol{n}$ of a fracture could be written as follows:

$$\boldsymbol{n} = -\sin\delta\sin\phi_s\boldsymbol{e}_N + \sin\delta\cos\phi_s\boldsymbol{e}_E + \cos\delta\boldsymbol{e}_U \quad (14)$$

where $\boldsymbol{e}_N$, $\boldsymbol{e}_E$ and $\boldsymbol{e}_U$ are the unit vectors in NEU coordinate, δ is the dip angle and ϕ_s is the strike. Accordingly, the dip ϕ_d can be derived. The orientations of the main fractures were subsequently projected to an equal-angle lower-hemisphere plot, as shown in Fig. 12. The colors of the fractures and the faults are preserved. The dip and dip angle of the main fracture in the hanging wall were 202.04°∠87.94°, respectively. The dip and dip angle of the main fracture in the foot wall were 189.78°∠59.22°, respectively. The rose diagram can be regarded as a 3D version of the stereographic diagram to some extent. Compared to the stereographic diagram, the rose diagram is intuitive to count and show the orientations of the fractures in 3D scenes.

[Fig. 12 goes here]

For shear and mixed-mode fractures, the surface that exhibited a smaller included angle with the main fracture was the real fracture plane. Here, the reference surface used to calculate the included angles was the selected main fracture rather than the fault. The main fracture was able to ensure that the generated fracture network had the same distribution regularity with the same main orientation. The fracture network was subsequently generated using MS data, as illustrated in Fig. 13. The resulting network exhibits realistic shapes of fracture growth patterns. The fractures were indicated by circular plates and colored according to the order of occurrence for the first row and the fracture volumes for the second row. The source radius and fracture aperture are the two important factors that affect the hydraulic conductivity. A fracture with a larger radius can connect with other fractures more easily, and vice versa. Meanwhile, a larger fracture aperture can significantly increase the hydraulic conductivity when a hydraulic source is connected. The source radii and fracture aperture were calculated using Eqs. (8) ~ (10). The white arrows illustrated the propagation paths of the fractures. The center area and the open-pit bottom were the two main places where the fractures initiated. Fractures in the center part were densely spaced with relatively small source radii (0 ~ 8 m) and moderate volumes (0.06 ~ 100 m^3). The rock mass was relatively intact prior to the onset of mining activities. Thus, few primary fractures were available to provide space for the rock mass to shear even if there were concentrated stresses. So the moment magnitudes therein were relatively small. In contrast, goaf No.3 was flooded for a long time before being detected. The illegal goaf had an irregular shape and was instable. Primary fractures were developed therein, and thus, it was easily disturbed by blasting. Then, fractures near the bottom and west sidewall of goaf No.3 had relatively high radii (5 ~ 15 m). Goaf No.3 easily connected with the center part and thereafter became the secondary hydraulic source. Fractures developed and expanded within the crown pillar during the monitoring period. Stresses from the slopes, water seepage, mining disturbances and fault activations made it unstable, making it require additional essential support. The fracture radii and fracture apertures near the fault were higher than those on either side. The fractures in the lower part of the network had medium radii and apertures, meaning that the seepage path was developing downward. Near the area, exposed fractures with water were found at the roof of the drift. The maximum water discharge rate in the drift once reached 5623 m^3/d. Consequently, preliminary reinforcement and waterproofing measures have been taken for the drift near this area. Boreholes with lengths of 2 m and diameters of 45 mm were drilled on the sidewall and roof of the drift. Waterproof material made of cement paste, sodium silicate and urea-formaldehyde resins was injected into the fractures through the boreholes by high-pressure grouting pumps. The water discharge rate was finally controlled blow 2240 m^3/d and the water could be pumped away in time.

[Fig. 13 goes here]

Field observations have been conducted to obtain the orientations of rock discontinuities in the same study area [49]. The results were presented in Fig. 14. There were three dominant sets of discontinuities S1, S2, and S3 in the pillar. It is interesting to find that the orientations of the main fractures, faults and the set S1 were quite close. It indicates there was some inner relationship between discontinuity set S1, fault dislocation and the mechanism of induced microseismicity. Considering a shear dislocation along the fault surfaces, discontinuities of similar orientations would promote the generation of MS events with similar focal mechanisms as a result of shear along the existing discontinuity surfaces. On the other hand, it also proves that the proposed method can efficiently determine the fracture surfaces of MS events.

[Fig. 14 goes here]

5.3 Overall damage analysis of the pillar

Mining-induced fractures have a significant effect on the rock mass strength and deformability. In order to assess the state of the crown pillar, a damage mechanical model is adopted to consider the effect of MS-derived fractures on the pillar. According to the damage theory of jointed rock mass, the overall damage tensor can be calculated as [50]:

$$\boldsymbol{\omega} = \sum_{k=1}^{N} \boldsymbol{\omega}^{\mathrm{k}} = \frac{l_{\mathrm{a}}}{V} \sum_{k=1}^{N} a^{\mathrm{k}} \left(\boldsymbol{n}^{\mathrm{k}} \otimes \boldsymbol{n}^{\mathrm{k}} \right) \tag{15}$$

where l_{a} is the average fracture spacing, V is the pillar volume, N is the fracture number, a^{k}, $\boldsymbol{\omega}^{\mathrm{k}}$ and $\boldsymbol{n}^{\mathrm{k}}$ are the area size, damage tensor and normal vector of the k-th fracture, respectively. The symbol $\otimes$ is tensor product.

The overall damage tensor of the pillar considering MS-derived fractures are shown in Fig. 15. The principal values of the damage tensor are d_i = [d_1, d_2, d_3] = [0.33, 0.12, 0.15]. The corresponding principal vectors are $\boldsymbol{\lambda}_1$=[0.96, -0.24, 0.14], $\boldsymbol{\lambda}_2$=[-0.26, -0.96, 0.13], $\boldsymbol{\lambda}_3$=[-0.11, 0.16, 0.98] in NEU coordinate system. The largest damage d_1 0.33 occurred in the north-south direction that is perpendicular to the fault. The damage value of d_1 is about two times larger than those in the other two principal directions. The strength and elastic modulus of the pillar in the direction perpendicular to the fault are the lowest. Disturbances like blasting and vibration from this direction would have the greatest influence on the stability of the pillar and deserved more attention. More rock bolts should be installed in this direction.

[Fig. 15 goes here]

6. MS-derived connected network analysis

Each MS event represents a fracture in the rock mass with a certain source radius and failure volume. The fractures were connected with one another, which is an important reason for the observed increase in the hydraulic conductivity. However, using only intersecting penny-shaped fractures as proxies to determine the seepage channels may greatly underestimate the number of seepage channels due to the ignorance of water seepage in rock mass. In this section, a fast chronological expansion method is proposed to build a connected network based on MS events and their source orientations, as an extension of the method from Hugot et al. [19]. It is applicable even if the MS events are sparsely distributed. Here we define two distances for an event, i.e., the impact distance l_i and the receptive distance l_r. Rock mass activities within l_i to a newly occurred event are very intense, so the new event is connected with the nearest existing fracture. In a distance from l_i to l_r, the fracture surface normal should be considered as a connection criterion. The included angle between the surface normal of the new event and the direction vector from event to event should be larger than β. In a distance larger than l_r, events would not be connected. Events are calculated and connected in chronological order, details of the building process are presented in Fig. 16. The blue and red circles in each step denote l_i and l_r, respectively.

[Fig. 16 goes here]

The results of the subsequent connected network of MS events are shown in Fig. 17. l_i, l_r and β are set to r_s, $2r_s$ and 60^o. The connections among MS-derived fractures form a seepage network in the pillar. In each step, a new MS event would be connected with the closest event that meet the connection criteria. It means that each connection bond can represent the shortest seepage path from the new MS event to the existing seepage networks. A small length denotes a strong bond, and vice versa. Additionally, bonds that were longer than the limiting distance L (L = 30 m in this case) were ignored. The bonds were classified into three types according to their lengths: 0 m ~ 6 m denoted a strong bond (0% ~ 20% of L), 6 m ~13.5 m denoted a medium bond (20% ~ 45% of L) and 13.5 m ~ 30 m denoted a weak bond (45% to 100% of L). In the study area, the bonds were generally distributed along the fault, and their lengths generally ranged from 1 m to 8 m. The strong bonds observed in the central part were dense and well developed, indicating that the fault was activated by mining activities. Beneath the northern bottom part of goaf No.3, strong bonds were clustered and connected with the central part. The crown pillar in the upper and western parts of the fault was full of strong and medium bonds. These bonds were connected with the water pool at the open-pit bottom, which constituted the main water recharge source. The roof of stope No.2 and the east sidewall of stope No.1 were the nearest areas of inrush from the central part. Strong bonds were also developed in the roof of the eastern part of the -60 m drift, and the nearby medium bonds extended downward and potentially affected the deeper working faces. During the monitoring period, goaf No.4 seemed to exhibit medium hydraulic bonds with the open-pit bottom and few bonds with the fault. Additionally, there was no precursor for the downward penetration of water within goaf No.4.

[Fig. 17 goes here]

7. Conclusions

We presented a microseismicity-based method to study the development of seepage channels. This method considers the chronological order and the focal mechanism of MS events in the inversion procedure of seepage channels. It is applicable even if the stress field is unspecified and MS events are sparsely distributed. The method was implemented to study the seepage channel development in the crown pillar beneath an open-pit to underground mining transition. The spatiotemporal evolution of the MS events, source mechanisms, fracture network, source radii, fault volumes, damage tensor and connected network were analyzed.

MS activities were very high in the crown pillar. The center area and the open-pit bottom were the two main places where the mining-induced fractures first initiated with small source radii and medium failure volumes. Fractures expanded as mining activities advanced to form the final seepage channels. Water from the open-pit bottom and upper goaf seeped downward along the fault and penetrated into the crown pillar. After gathering within the center part of the faults, most of the water flowed downward into stope No.2. Two main hydraulic recharge sources and three discharge points were localized. The seepage channels between hydraulic recharge and discharge points were inferred.

Shear fractures were dominant in the crown pillar and accounted for more than 90% of all MS events. As the MS events are induced by the fault activation under disturbances from mining, a similar mechanism assumption was made to determine the fracture surfaces of non-tensile MS events. MS-derived fractures with average orientations of $202.04^{o}\angle 87.94^{o}$ and $189.78^{o}\angle 59.22^{o}$ were obtained in the hanging wall and footwall of the faults, respectively. A set of discontinuities with similar orientations were obtained by field observations in the pillars. The existence of the discontinuities was found to be an important factor affecting the focal mechanism of the MS events besides the mining activities. The overall damage state of the pillar was assessed based on the MS-derived fracture network. The direction with the largest damage value was approximately perpendicular to the faults. Mining-induced fractures compromised the overall stability of the crown pillar, which could form seepage channels and might subsequently lead to water inrush.

A fast chronological expansion method was proposed to build a connected network based on MS locations and their source orientations obtained from MTI. The approach provided a convenient way to efficiently reveal the pattern of seepage channels. The distances of event-to-event seepage were estimated and the shortest seepage channel from each individual event to the network was determined in chronological order.

Although the approach provides a convenient way to perform seepage channel development analysis, the method is highly dependent on high-quality seismic records. Poor-quality, unreliable and non-representative events should be carefully eliminated. MS event location is the second factor that has a serious impact on the reliability of results. Precise location of MS event in a complex engineering rock mass is challenging so far. Ray-tracing based locating method might be helpful to improve the accuracy of the connected network.

Declaration of competing interest

The authors declared that they have no conflicts of interest to this work.

Acknowledgements

We acknowledge the combined support from the China Postdoctoral Science Foundation (2019M663502) and the National Science Foundation of China (52039007).

References

1. Ghasemi E, Kalhori H, Bagherpour R. Stability assessment of hard rock pillars using two intelligent classification techniques: A comparative study. *Tunnelling and Underground Space Technology.* 2017;68: 32-37.
2. Esterhuizen GS, Dolinar DR, Ellenberger JL. Pillar strength in underground stone mines in the United States. *International Journal of Rock Mechanics and Mining Sciences.* 2011;48(1): 42-50.

3. Galvin J. Considerations Associated with the Application of the UNSW and Other Pillar Design Formulae. *Golden Rocks 2006, The 41st U.S. Symposium on Rock Mechanics (USRMS).* Golden, Colorado: American Rock Mechanics Association; 2006:9.

4. Poulsen BA. Coal pillar load calculation by pressure arch theory and near field extraction ratio. *International Journal of Rock Mechanics and Mining Sciences.* 2010;47(7): 1158-1165.

5. Ghasemi E, Shahriar K. A new coal pillars design method in order to enhance safety of the retreat mining in room and pillar mines. *Safety Science.* 2012;50(3): 579-585.

6. Martin CD, Maybee WG. The strength of hard-rock pillars. *International Journal of Rock Mechanics and Mining Sciences.* 2000;37(8): 1239-1246.

7. Lunder P, Pakalnis R. Determination of the strength of hard-rock mine pillars. *World Mining Express.* 1998;14(4): 24-28.

8. Tawadrous AS, Katsabanis PD. Prediction of surface crown pillar stability using artificial neural networks. *International Journal for Numerical and Analytical Methods in Geomechanics.* 2007;31(7): 917-931.

9. Zaidel J, Markham B, Bleiker D. Simulating Seepage into Mine Shafts and Tunnels with MODFLOW. *Groundwater.* 2010;48(3): 390-400.

10. Yang TH, Wang PT, Xu T, et al. Anisotropic characteristics of jointed rock mass: A case study at Shirengou iron ore mine in China. *Tunnelling & Underground Space Technology.* 2015;48: 129-139.

11. Liu Y-C, Chen C-S. A new approach for application of rock mass classification on rock slope stability assessment. *Engineering Geology.* 2007;89(1): 129-143.

12. Feng GL, Feng XT, Chen BR, Xiao YX. Performance and feasibility analysis of two microseismic location methods used in tunnel engineering. *Tunnelling and Underground Space Technology.* 2017;63: 183-193.

13. Xiao YX, Feng XT, Chen BR, Feng GL, Yao ZB, Hu LX. Excavation-induced microseismicity in the columnar jointed basalt of an underground hydropower station. *International Journal of Rock Mechanics and Mining Sciences.* 2017;97: 99-109.

14. Li B, Xu N, Dai F, Zhang G, Xiao P. Dynamic analysis of rock mass deformation in large underground caverns considering microseismic data. *International Journal of Rock Mechanics and Mining Sciences.* 2019;122: 104078.

15. Xu NW, Dai F, Liang ZZ, Zhou Z, Sha C, Tang CA. The dynamic evaluation of rock slope stability considering the effects of microseismic damage. *Rock Mechanics and Rock Engineering.* 2014;47(2): 621-642.

16. Salvoni M, Dight PM. Rock damage assessment in a large unstable slope from microseismic monitoring - MMG Century mine (Queensland, Australia) case study. *Engineering Geology.* 2016;210: 45-56.

17. Ma K, Tang CA, Liang ZZ, Zhuang DY, Zhang QB. Stability analysis and reinforcement evaluation of high-steep rock slope by microseismic monitoring. *Engineering Geology.* 2017;218: 22-38.

18. Dai F, Jiang P, Xu N, Chen W, Tan Y. Focal mechanism determination for microseismic events and its application to the left bank slope of the Baihetan hydropower station in China. *Environmental Earth Sciences.* 2018;77(7): 268.

19. Hugot A, Dulac J-C, Gringarten E, Haouesse A. Connecting the Dots: Microseismic-Derived Connectivity for Estimating Volumes in Low-Permeability Reservoirs. *Unconventional Resources Technology Conference.* San Antonio, Texas, USA: Unconventional Resources Technology Conference; 2015:12.

20. Kushnir A, Varypaev A. Robustness of statistical algorithms for location of microseismic sources based on surface array data. *Computational Geosciences.* 2017;21(3): 459-477.

21. Chen H, Meng X, Niu F, Tang Y, Yin C, Wu F. Microseismic Monitoring of Stimulating Shale Gas Reservoir in SW China: 2. Spatial Clustering Controlled by the Preexisting Faults and Fractures. *Journal of Geophysical Research: Solid Earth.* 2018;123(2): 1659-1672.

22. Fairhurst C. Nuclear waste disposal and rock mechanics: contributions of the Underground Research Laboratory (URL), Pinawa, Manitoba, Canada. *International Journal of Rock Mechanics and Mining Sciences.* 2004;41(8): 1221-1227.

23. Martino JB, Chandler NA. Excavation-induced damage studies at the Underground Research Laboratory. *International Journal of Rock Mechanics and Mining Sciences.* 2004;41(8): 1413-1426.

24. Cheng G, Li L, Zhu W, et al. Microseismic investigation of mining-induced brittle fault activation in a Chinese coal mine. *International Journal of Rock Mechanics and Mining Sciences.* 2019;123: 104096.

25. Zhao Y, Yang T, Zhang P, Xu H, Wang S. Inversion of seepage channels based on mining-induced microseismic data. *International Journal of Rock Mechanics and Mining Sciences.* 2020;126: 104180.

26. Ma K, Sun XY, Tang CA, Yuan FZ, Wang SJ, Chen T. Floor water inrush analysis based on mechanical failure characters and microseismic monitoring. *Tunnelling and Underground Space Technology.* 2020: 103698.

27. Tang CA, Wang JM, Zhang JJ. Preliminary engineering application of microseismic monitoring technique to rockburst prediction in tunneling of Jinping Ⅱ project. *Journal of Rock Mechanics and Geotechnical Engineering.* 2010;2(3): 193-208.

28. Xiao YX, Feng XT, Hudson JA, Chen BR, Feng GL, Liu JP. ISRM suggested method for in situ microseismic monitoring of the fracturing process in rock masses. *Rock Mechanics and Rock Engineering.* 2016;49(1): 343-369.

29. Li T, Mei TT, Sun XH, Lv YG, Sheng JQ, Cai M. A study on a water-inrush incident at Laohutai coalmine. *International Journal of Rock Mechanics and Mining Sciences.* 2013;59: 151-159.

30. Zhang PH, Yang TH, Yu QL, et al. Microseismicity induced by fault activation during the fracture process of a crown pillar. *Rock Mechanics and Rock Engineering.* 2015;48(4): 1673-1682.

31. Zhang S, Guo W, Li Y, Sun W, Yin D. Experimental Simulation of Fault Water Inrush Channel Evolution in a Coal Mine Floor. *Mine Water and the Environment.* 2017;36(3): 443-451.

32. Shi W, Yang T, Yu Q, Li Y, Liu H, Zhao Y. A Study of Water-Inrush Mechanisms Based on Geo-Mechanical Analysis and an In-situ Groundwater Investigation in the Zhongguan Iron Mine, China. *Mine Water and the Environment.* 2017;36(3): 409-417.

33. Feignier B, Young RP. Moment tensor inversion of induced microseisnmic events: Evidence of non-shear failures in the $-4 < M < -2$ moment magnitude range. *Geophysical Research Letters.* 1992;19(14): 1503-1506.

34. Linzer LM. A Relative Moment Tensor Inversion Technique Applied to Seismicity Induced by Mining. *Rock Mechanics and Rock Engineering.* 2005;38(2): 81-104.

35. Aki K, Richards PG. *Quantitative seismology, second edition*: University Science Books; 2002.

36. Ohtsu M. *Moment tensor analysis*: Springer Berlin Heidelberg; 2008.

37. Knopoff L, Randall MJ. The compensated linear-vector dipole: A possible mechanism for deep earthquakes. *Journal of Geophysical Research (1896-1977).* 1970;75(26): 4957-4963.

38. Fitch TJ, McCowan DW, Shields MW. Estimation of the seismic moment tensor from teleseismic

body wave data with applications to intraplate and mantle earthquakes. *Journal of Geophysical Research: Solid Earth.* 1980;85(B7): 3817-3828.

39. Mendecki DAJ. *Seismic monitoring in mines*: Chapman & Hall; 1997.

40. Akaike H. Markovian representation of stochastic processes and its application to the analysis of autoregressive moving average processes. *Annals of the Institute of Statistical Mathematics*. 1974;26(1): 363-387.

41. Liu H, Zhang J. STA/LTA algorithm analysis and improvement of Microseismic signal automatic detection. *Progress in Geophysics.* 2014;29(4): 1708-1714.

42. Geiger L. Probability method for the determination of earthquake epicenters from the arrival time only. *Bulletin of Saint Louis University.* 1912;8(1): 60-71.

43. Zhou JR, Yang TH, Zhang PH, Xu T, Wei J. Formation process and mechanism of seepage channels around grout curtain from microseismic monitoring: A case study of Zhangmatun iron mine, China. *Engineering Geology.* 2017;226: 301-315.

44. Kao CS, Carvalho FCS, Labuz JF. Micromechanisms of fracture from acoustic emission. *International Journal of Rock Mechanics and Mining Sciences.* 2011;48(4): 666-673.

45. Mahdevari S, Shahriar K, Sharifzadeh M, Tannant DD. Assessment of failure mechanisms in deep longwall faces based on mining-induced seismicity. *Arabian Journal of Geosciences.* 2016;9(18): 709.

46. Vavryčuk V. Iterative joint inversion for stress and fault orientations from focal mechanisms. *Geophysical Journal International*. 2014;199(1): 69-77.

47. Hardebeck JL, Michael AJ. Damped regional-scale stress inversions: Methodology and examples for southern California and the Coalinga aftershock sequence. *Journal of Geophysical Research: Solid Earth.* 2006;111(B11).

48. Capuano P, Zollo A, Singh SK. Source characteristics of moderate size events using empirical Green funclions: an application to some Guerrero (Mexico) subduction zone earthquakes. *Annals of Geophysics.* 1994;37(6): 1659-1677.

49. Zhou JR, Wei J, Yang TH, Zhu WC, Li LC, Zhang PH. Damage analysis of rock mass coupling joints, water and microseismicity. *Tunnelling and Underground Space Technology.* 2018;71: 366-381.

50. Liu H, Yuan X. A damage constitutive model for rock mass with persistent joints considering joint shear strength. *Canadian Geotechnical Journal*. 2015;52(8): 1136-1143.

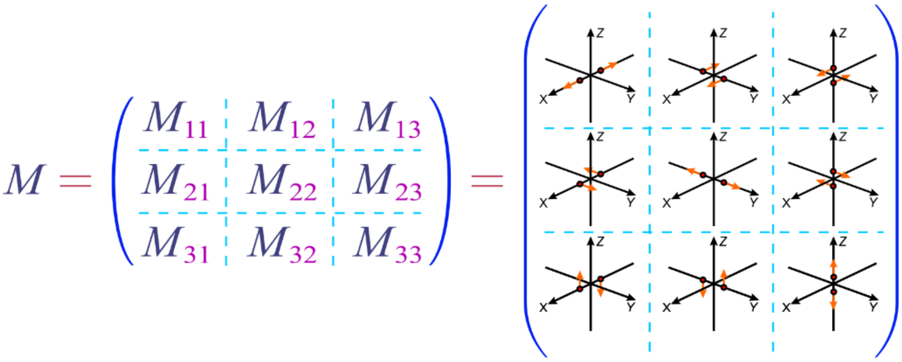

Fig. 1 Components of a moment tensor

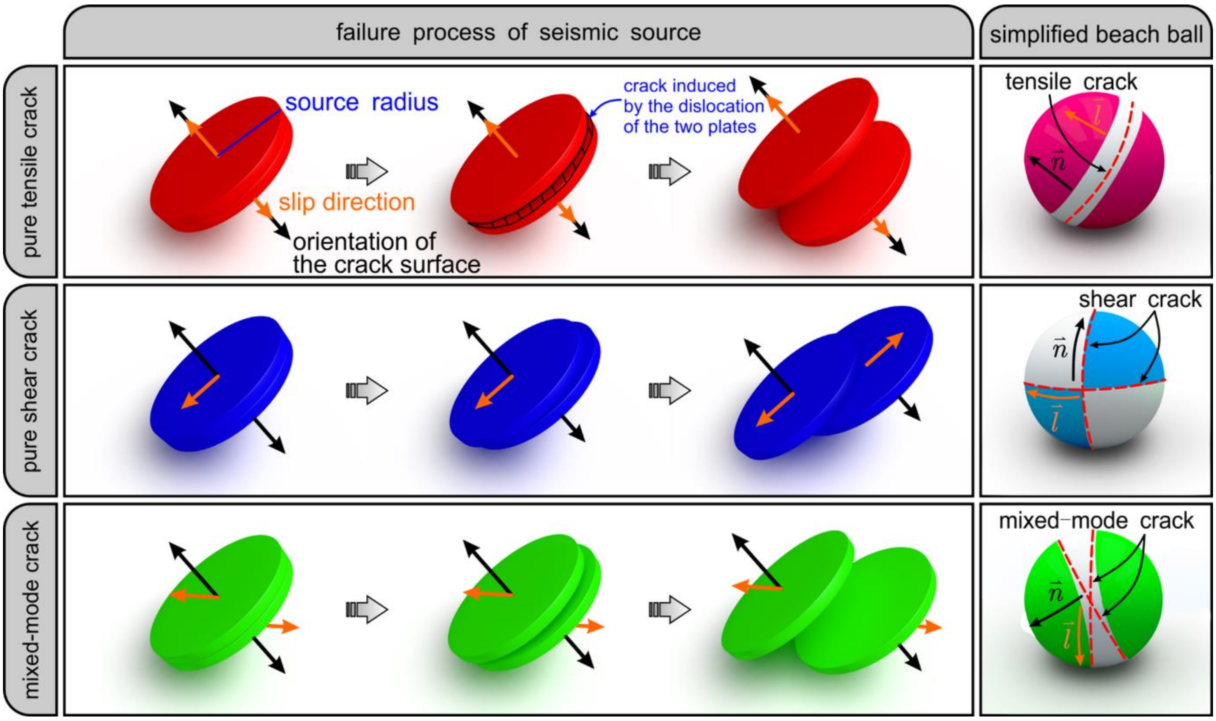

Fig. 2 Failure process and characterization of microseismic sources

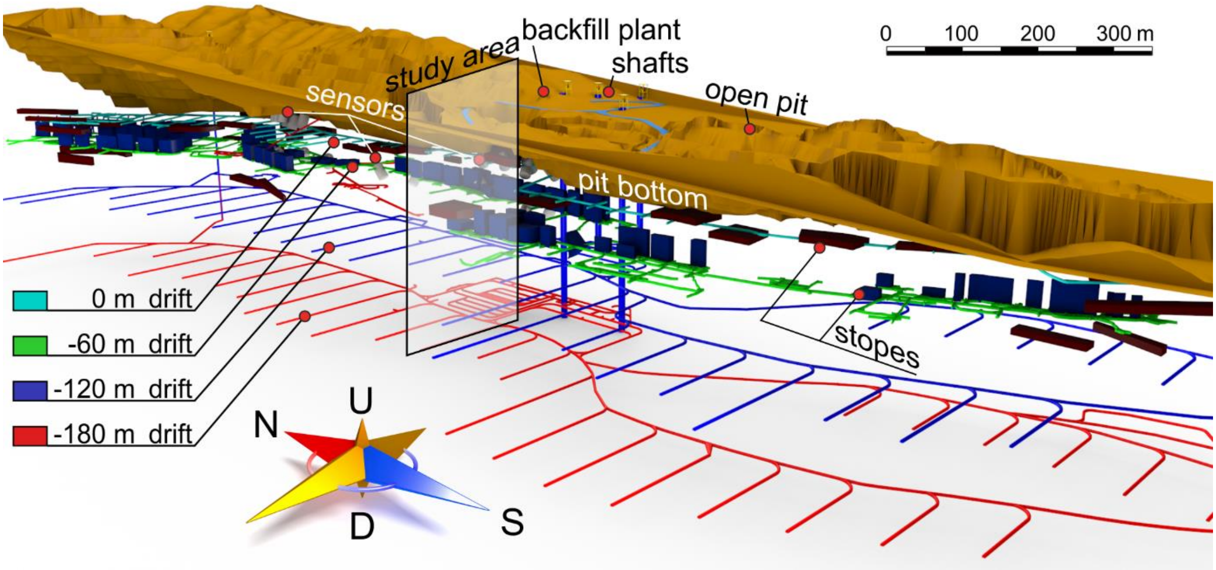

Fig. 3 Diagram of the mine. The abbreviations N, S, U and D near the compass represent north, south, up and down, respectively

Fig. 4 Photograph of the study area

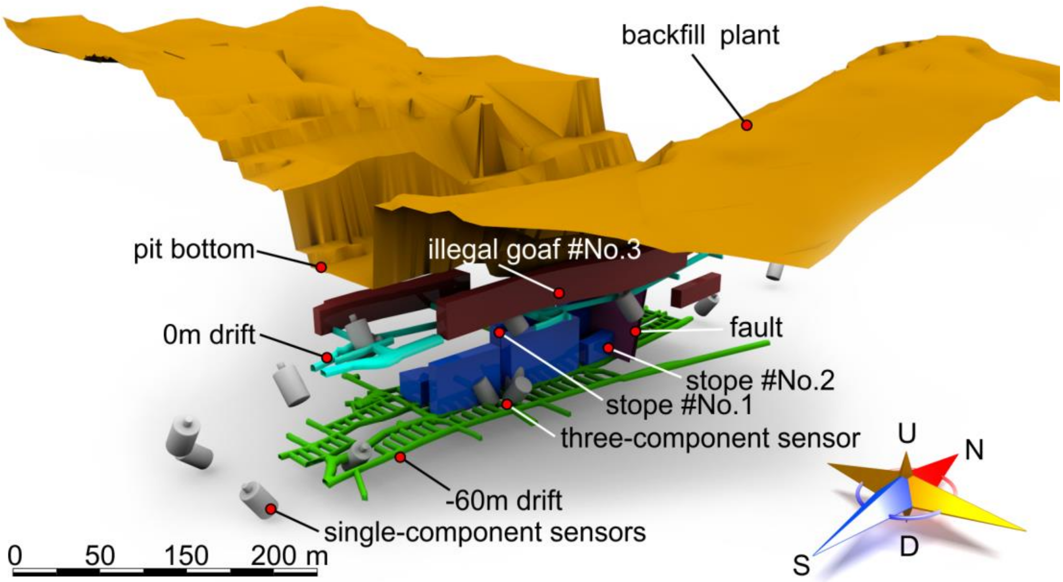

Fig. 5 Diagram of the study area and sensor array. Blue (■) and brown (■) blocks below the surface denote stopes, and the cyan (■) and green (■) tunnels represent 0 m and -60 m drifts, respectively

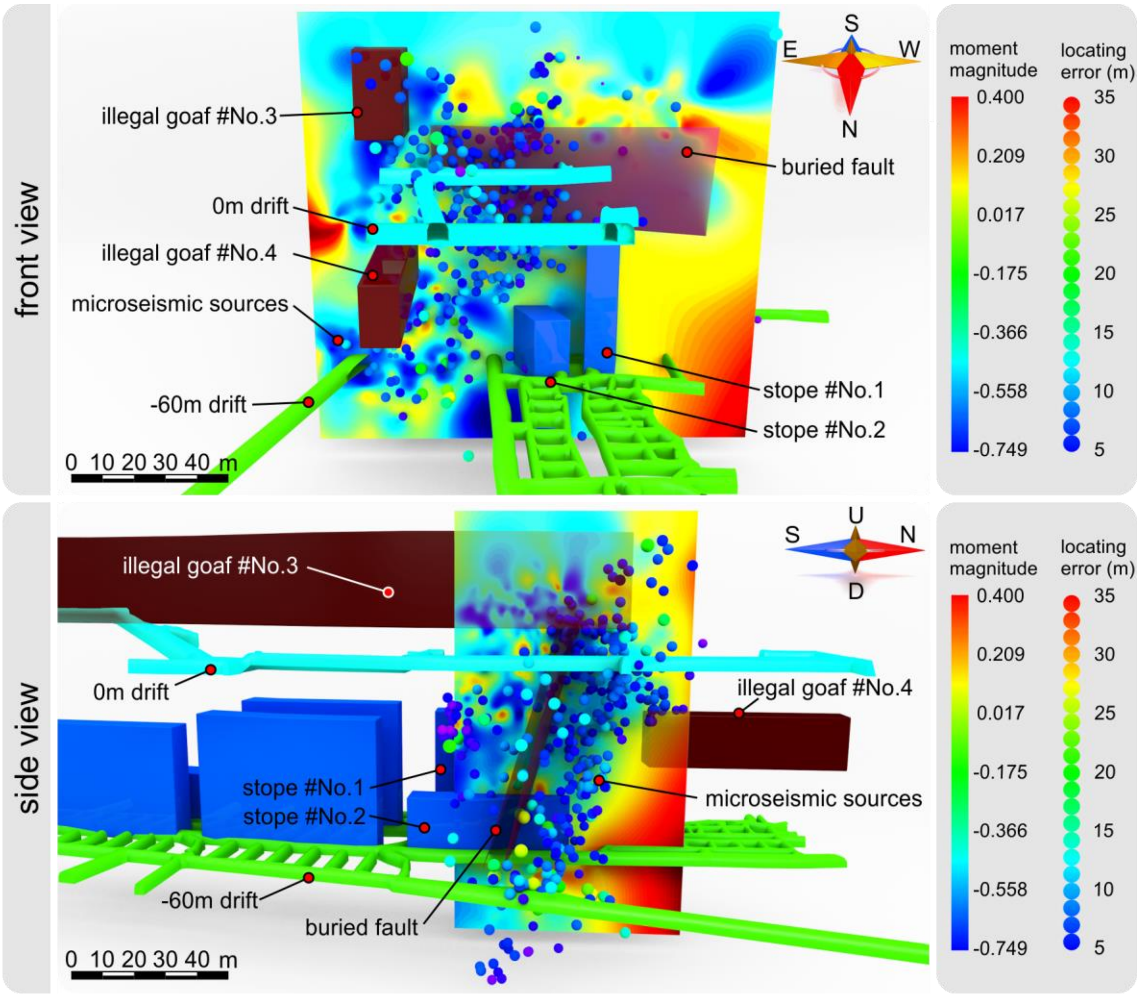

Fig. 6 Location error distribution for the MS events. Events are colored according to the moment magnitude and the distribution of the location error is shown in the colored map

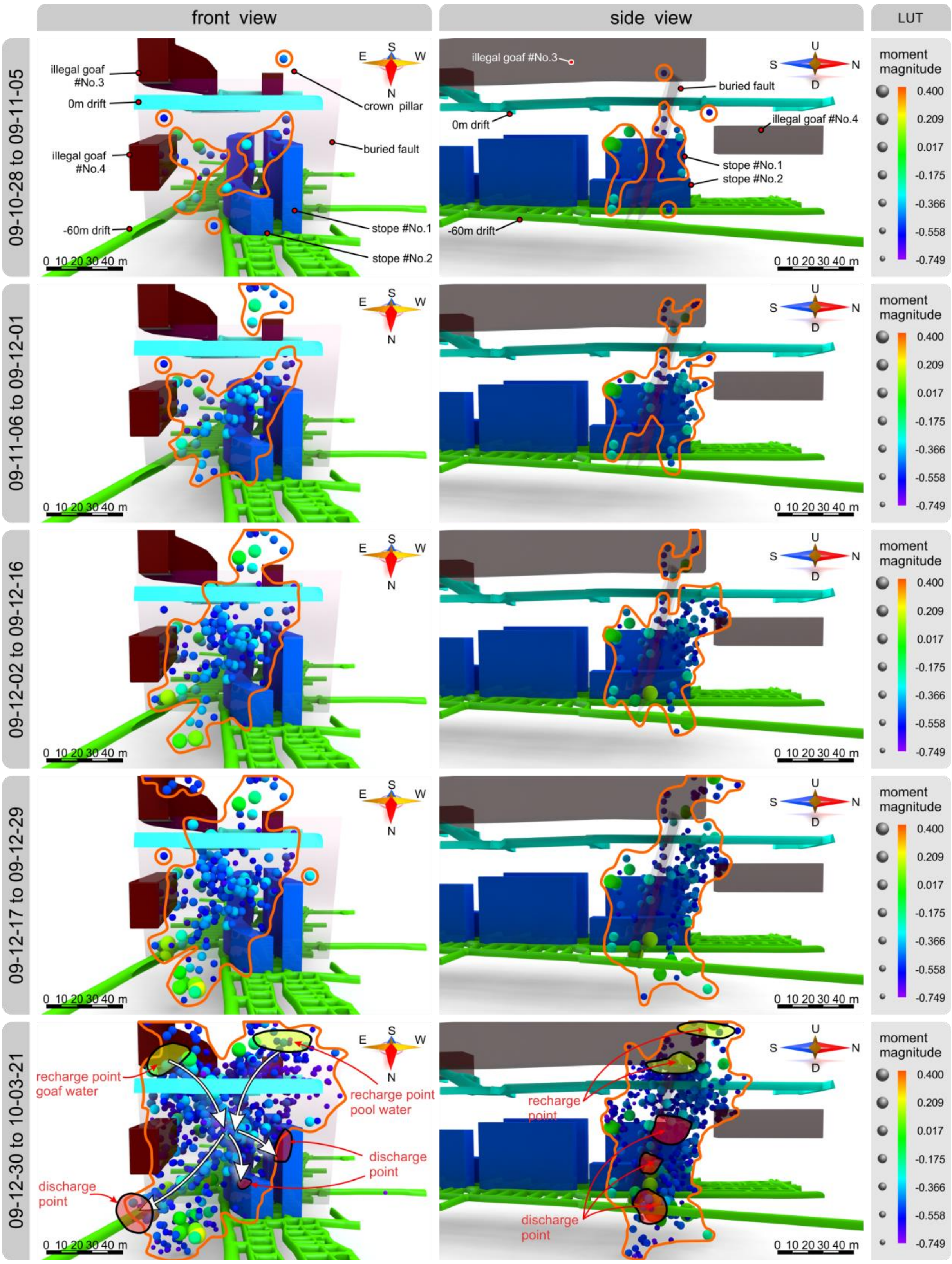

Fig. 7 Spatiotemporal evolution of the MS events

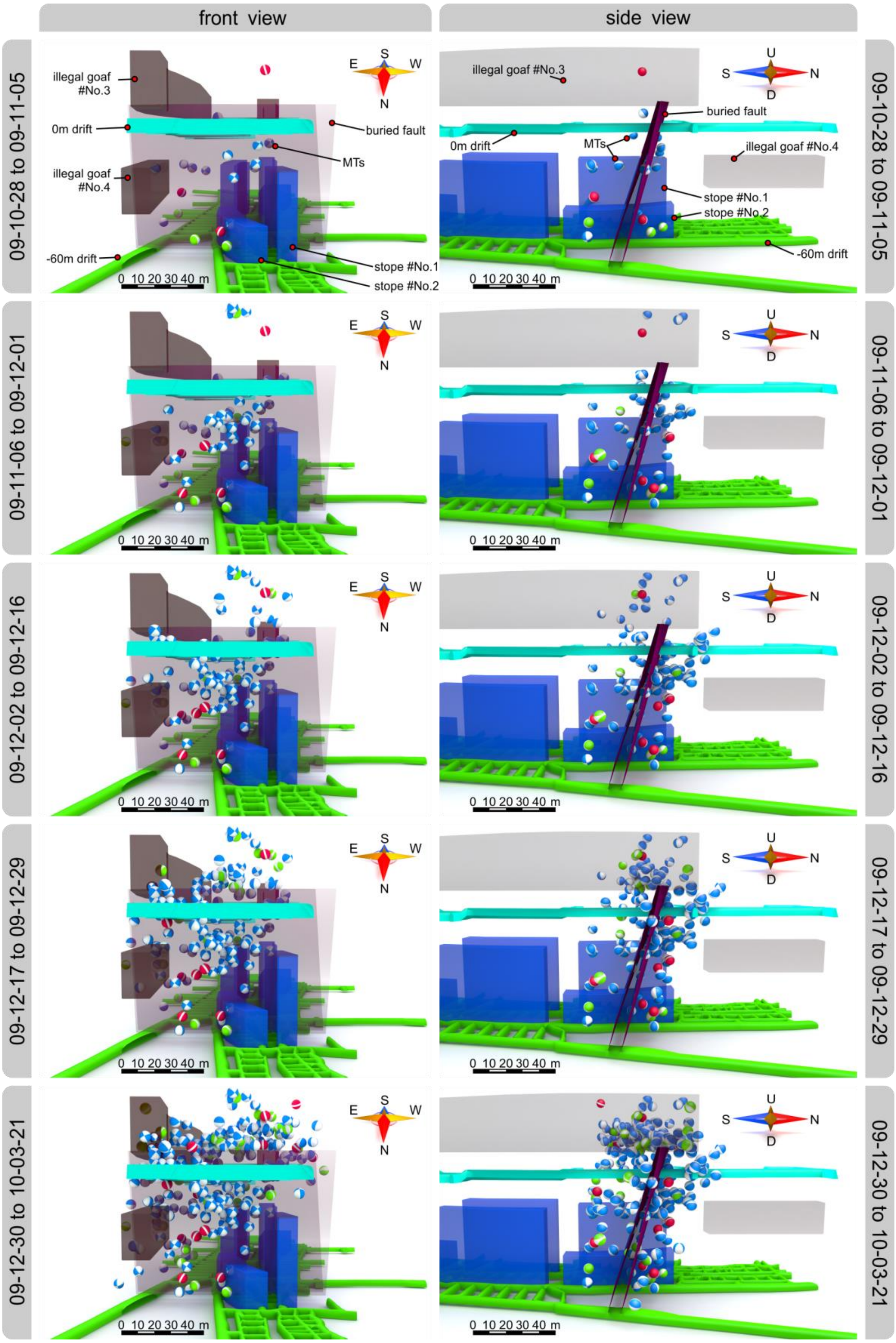

Fig. 8 Spatiotemporal evolution of MT beach balls in the study area. Red, green and blue beach balls represent tensile, mixed-mode and shear fractures, respectively

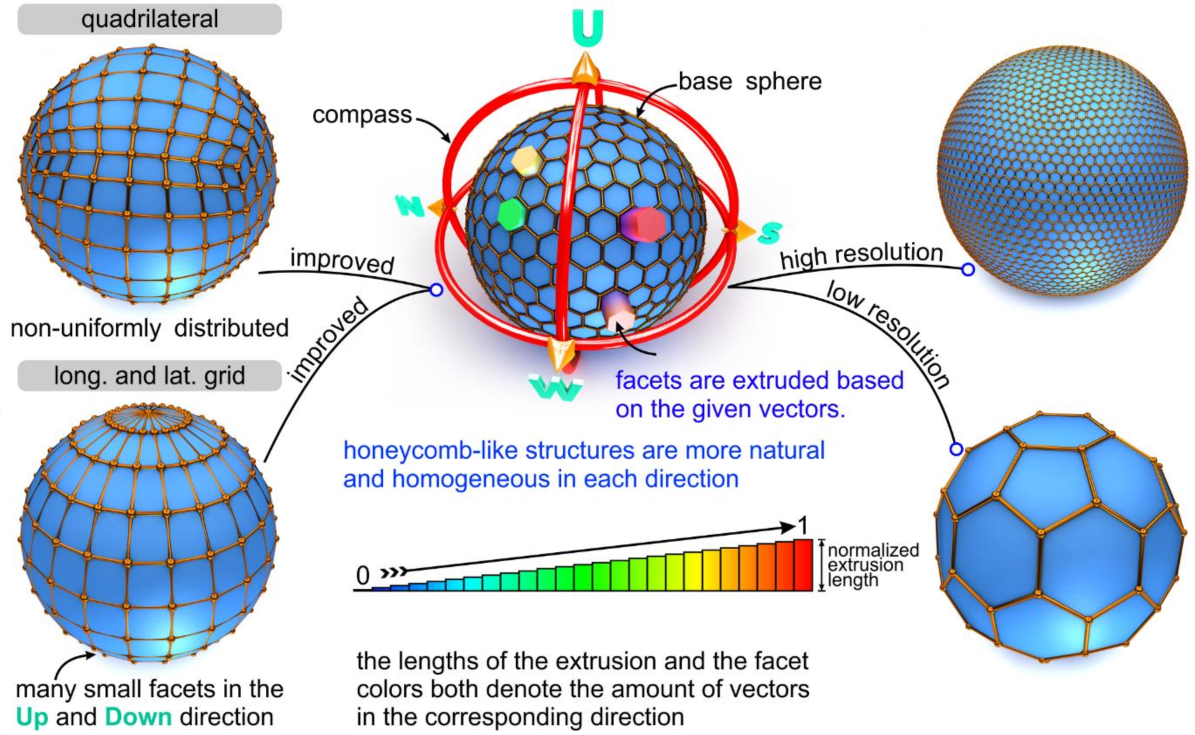

Fig. 9 Illustration of a 3D rose diagram

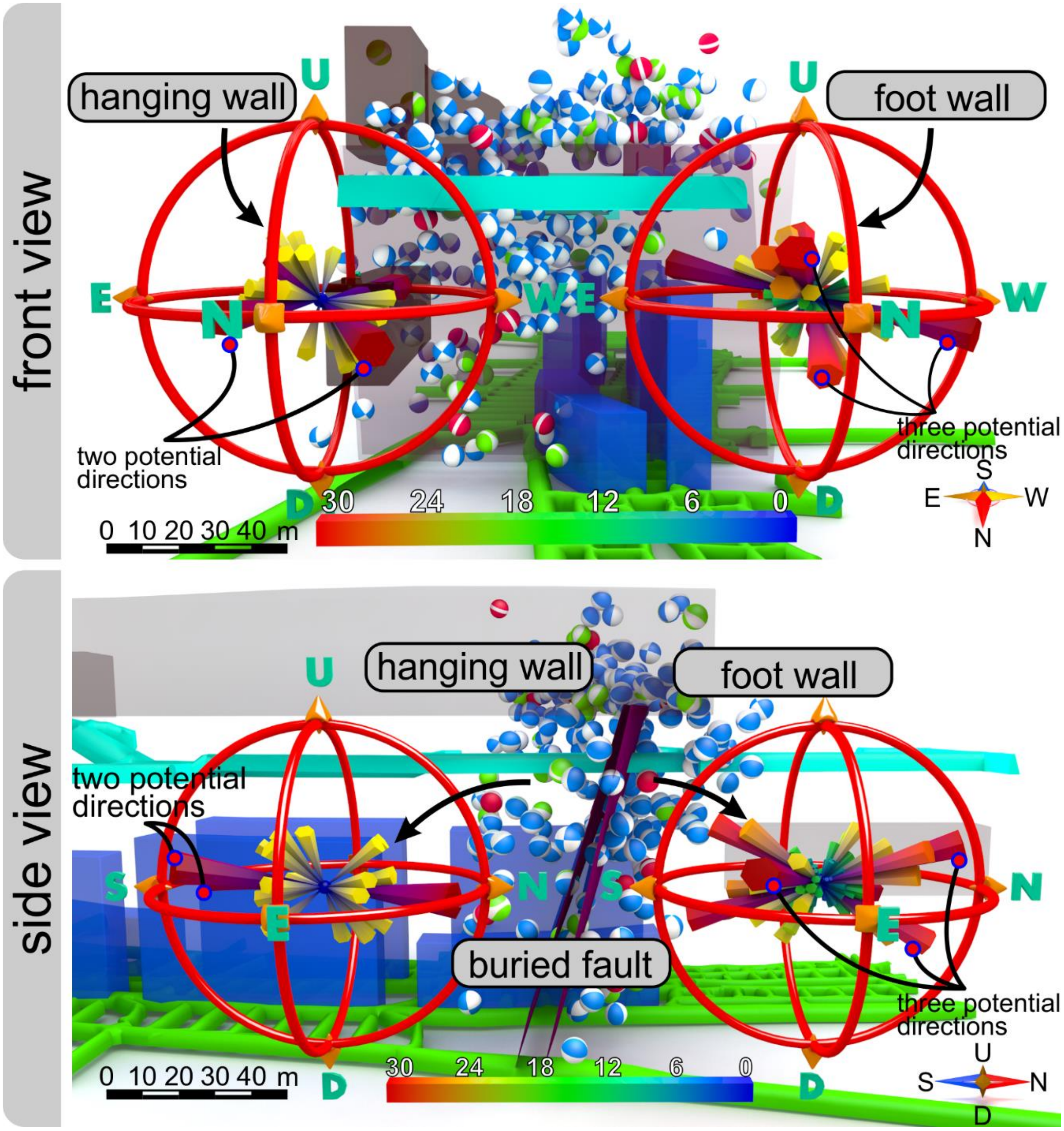

Fig. 10 3D rose diagrams of the normal vectors of fracture surfaces. The left diagram represents the fracture normal distribution in hanging wall, and the right diagram represents fracture normal distribution in the foot wall

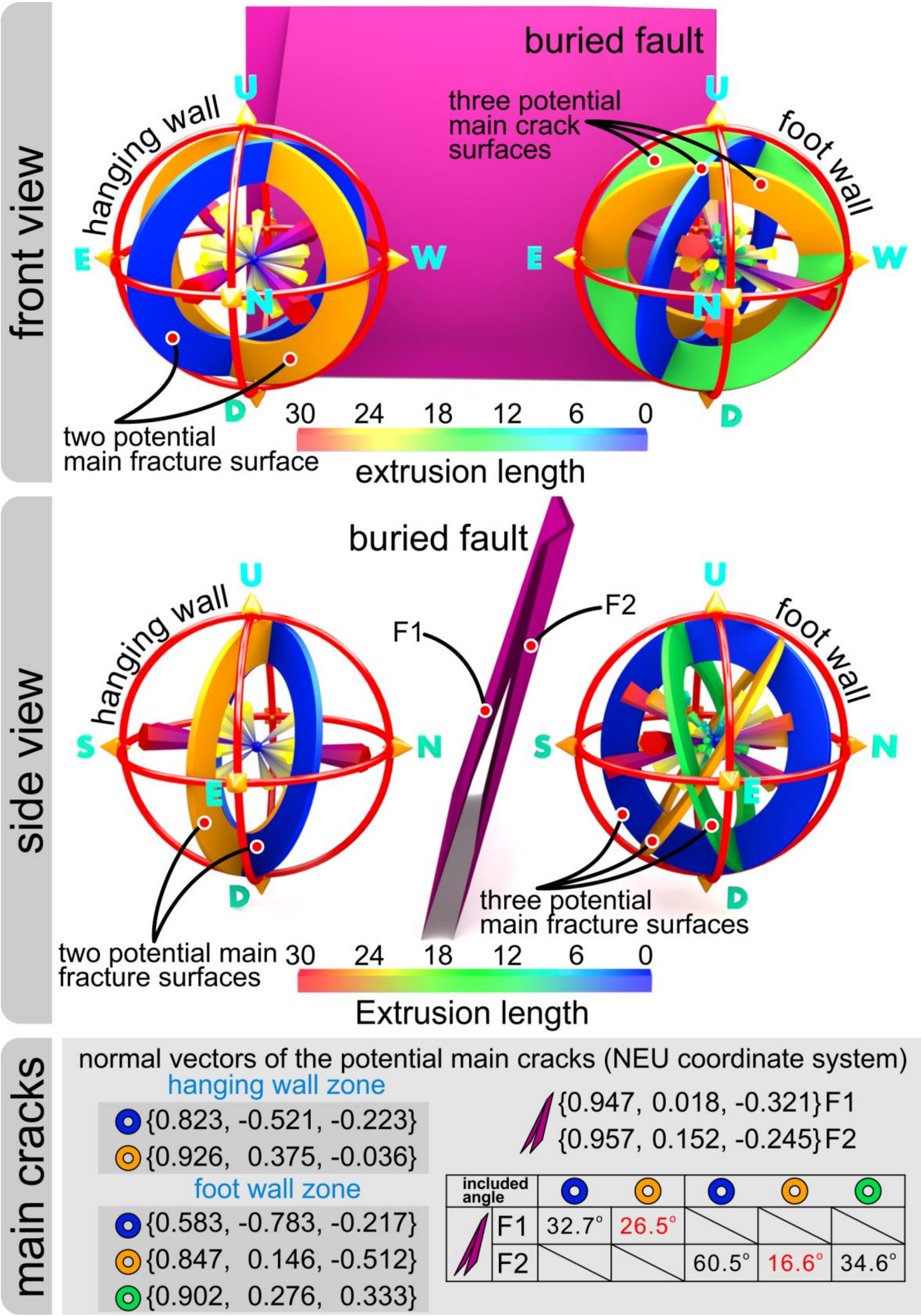

Fig. 11 Determination of the main fracture surfaces on either side of the buried fault

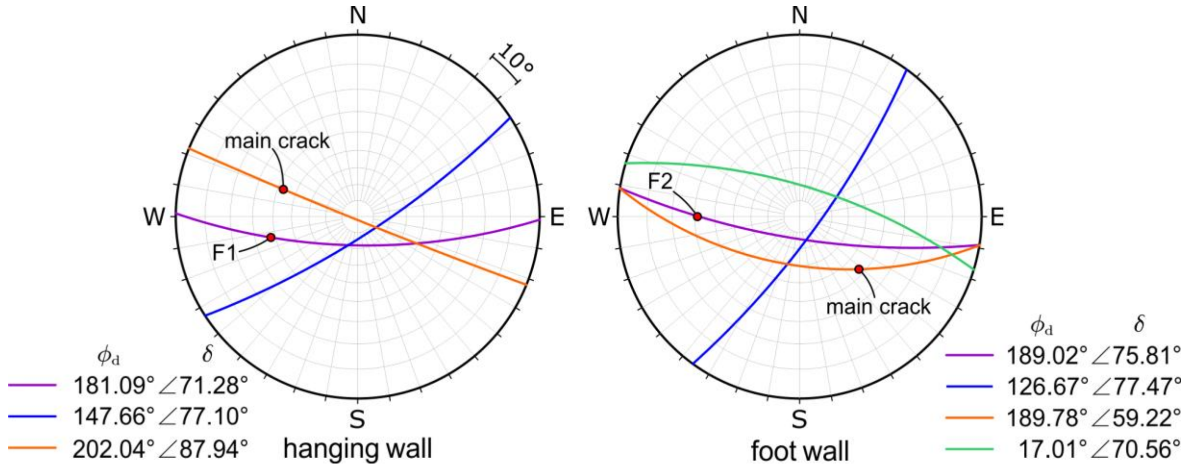

Fig. 12 Stereographic projection of the orientations of the main fractures in the hanging wall (left) and foot wall (right)

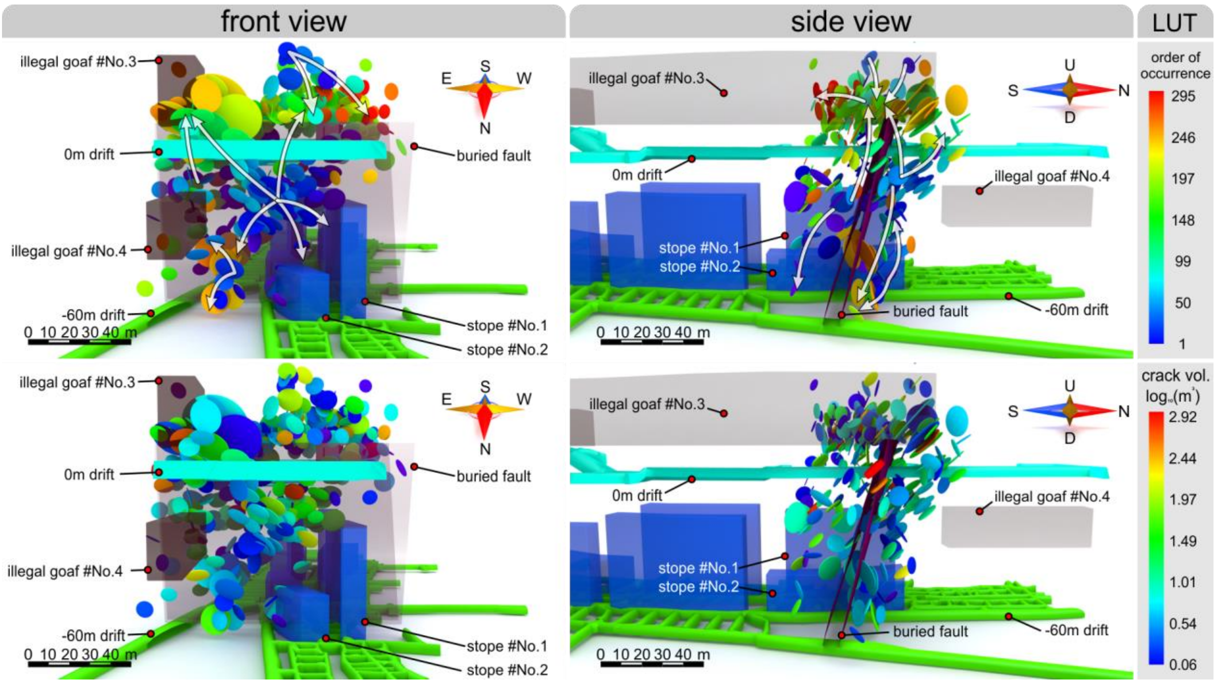

Fig. 13 Microseismic-derived fracture network in the pillars

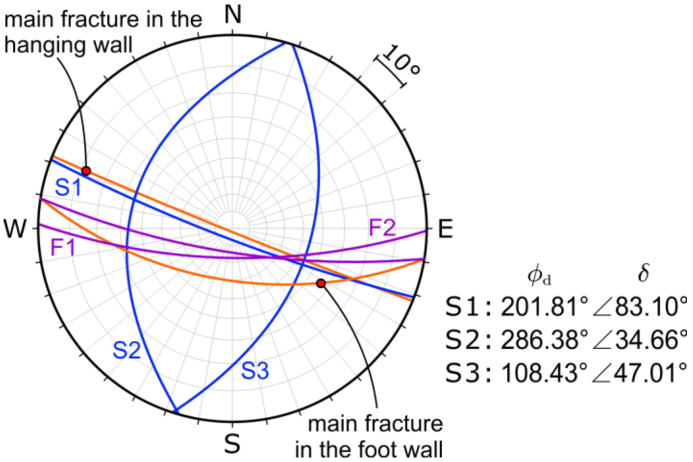

Fig. 14 Stereographic projection of the orientations of the sets of discontinuities S1, S2 and S3 in the pillar

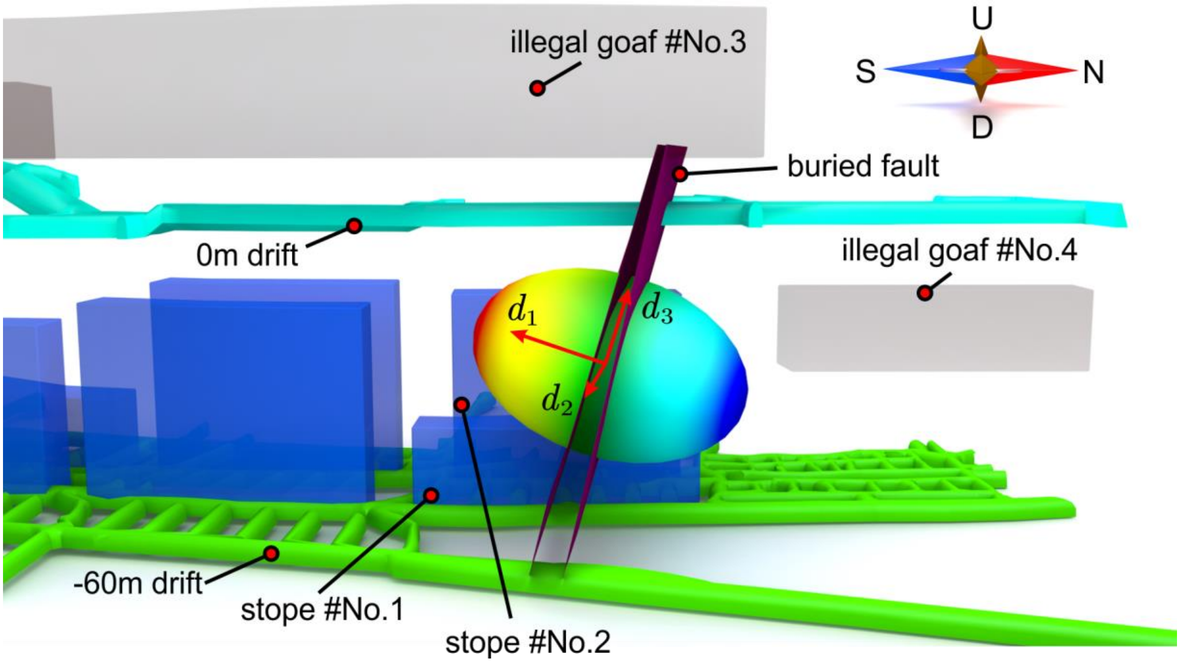

Fig. 15 Damage tensor of the pillar considering microseismic-derived fractures. The ellipsoid illustrates the damage tensor and the red arrows denote the principal directions of the damage tensor

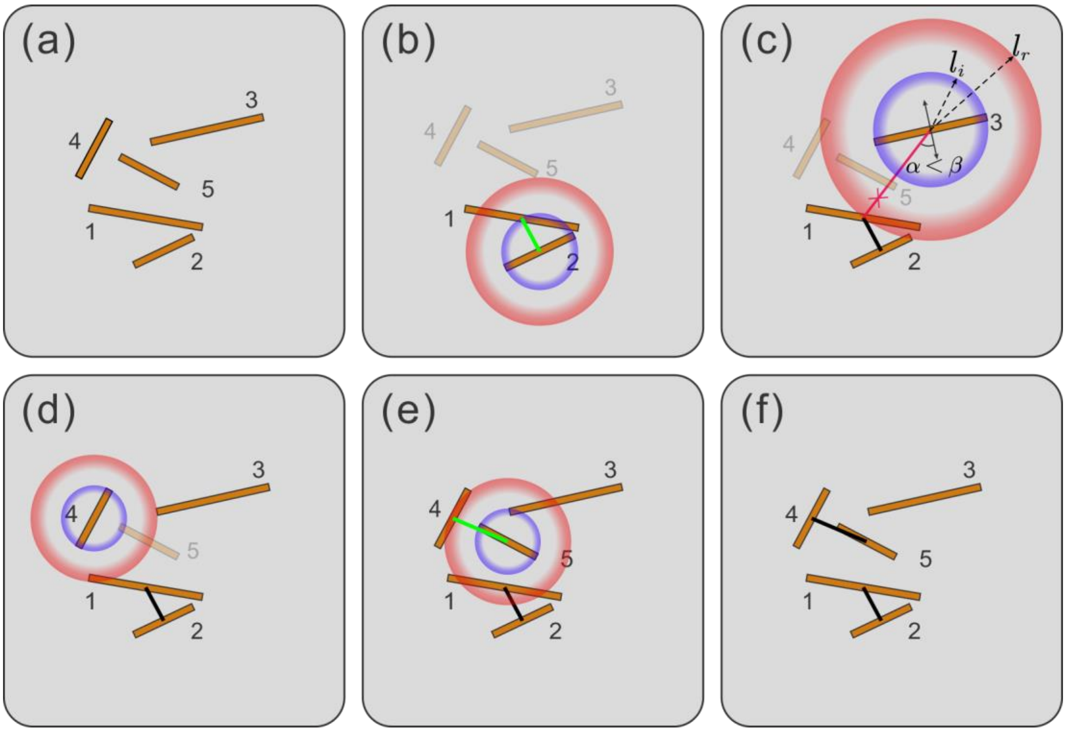

Fig. 16 Schematic view of chronological expansion of event connections. (a) Distribution of MS-derived fractures; (b) Connection within impact distance; (c) The angle is not enough to make a connection; (d) No event found within the receptive distance; (e) Make a connection when the angle criterion is satisfied; (f) Result of a connection network. Impact distance, receptive distance and β in the sketch map are set to source radius r_s, $1.9r_s$ and 70° respectively

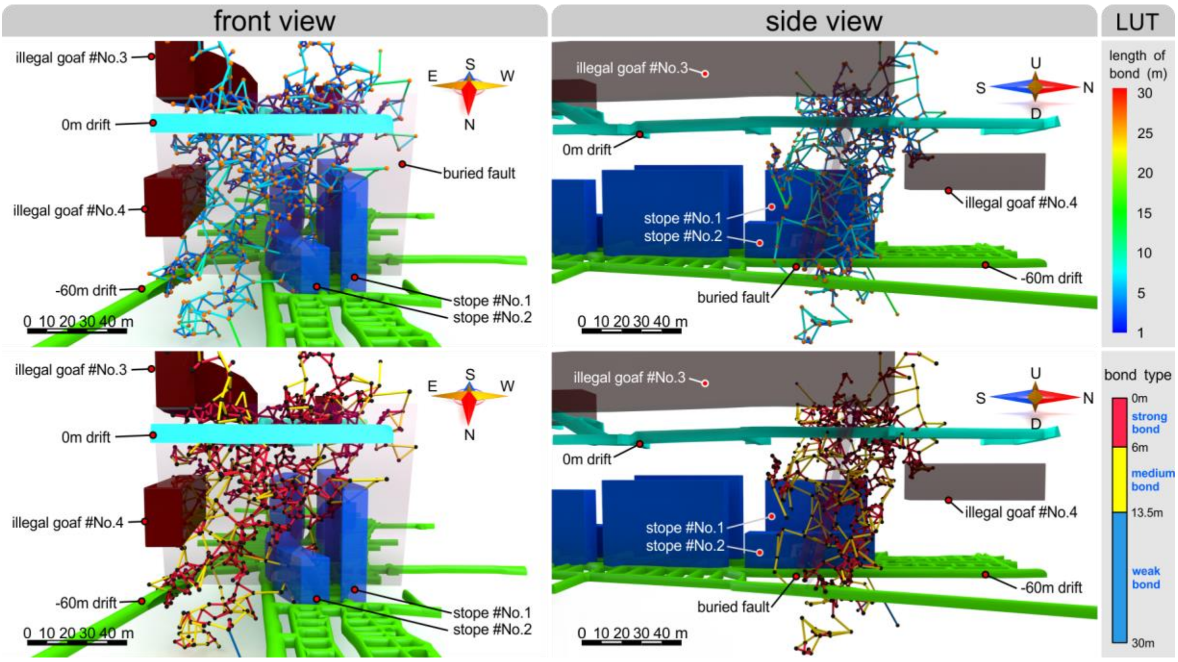

Fig. 17 MS-derived connected network in the pillars

Declaration of competing interest

The authors declared that they have no conflicts of interest to this work.